Journal of Applied Physics

Inverted hysteresis as a diagnostic tool for perovskite solar cells: Insights from the drift-diffusion model

Cite as: J. Appl. Phys. **133**, 095001 (2023); https://doi.org/10.1063/5.0136683
Submitted: 28 November 2022 • Accepted: 10 February 2023 • Published Online: 01 March 2023
Published open access through an agreement with JISC Collections

Will Clarke, Matthew V. Cowley, Matthew J. Wolf, et al.

AIP Publishing

Journal of Applied Physics ARTICLE scitation.org/journal/jap

Inverted hysteresis as a diagnostic tool for perovskite solar cells: Insights from the drift-diffusion model

Cite as: J. Appl. Phys. **133**, 095001 (2023); doi: 10.1063/5.0136683
Submitted: 28 November 2022 · Accepted: 10 February 2023 ·
Published Online: 1 March 2023

Will Clarke,[1,a)] Matthew V. Cowley,[2,3] Matthew J. Wolf,[4] Petra Cameron,[2,3] Alison Walker,[5] and Giles Richardson[1]

AFFILIATIONS

[1]Mathematical Sciences, University of Southampton, Southampton, UK
[2]Centre for Sustainable and Circular Technologies, University of Bath, Bath, UK
[3]Department of Chemistry, University of Bath, Bath, UK
[4]Institute of Physical Chemistry, RWTH Aachen University, Aachen, Germany
[5]Department of Physics, University of Bath, Bath, UK

[a)]**Author to whom correspondence should be addressed:** wc3g16@soton.ac.uk

ABSTRACT

Despite current–voltage hysteresis in perovskite solar cells (PSCs) having been the subject of significant research over the past decade, inverted hysteresis (IH), although frequently observed, is still not properly understood. Several mechanisms, based on numerical simulations, have been proposed to explain it but a satisfactory description of the underlying cause remains elusive. To rectify this omission, we analyze a drift-diffusion model of a planar three-layer PSC, using asymptotic techniques, to show how inverted hysteresis comes about. The asymptotic analysis of the drift-diffusion model yields a simple approximate model that shows excellent agreement with numerical simulations of the full drift-diffusion model provides fundamental insights into the causes of IH and reconciles the alternative explanations found in the literature. This approximate model is analyzed further to isolate the material properties and external conditions that contribute to inverted hysteresis and constitutes a diagnostic tool in which the appearance of IH can be used to infer properties of the cell.

I. BACKGROUND

A. Development of PSCs

Perovskite solar cells (PSCs) have received tremendous attention from the photovoltaics community over the past decade, as their power conversion efficiencies (PCEs) have climbed to be comparable to that of silicon solar cells (see, e.g., Ref. 1), the current market leader. In 2012, efficiencies began to cross the 10% threshold,[2,3] sparking a significant research effort in the understanding and development of these devices. PSCs quickly became the fastest growing PV technology in terms of PCE, with a current record of 25.7%.[4] Another attractive benefit of PSCs is the possibility of cheap large-scale manufacturing, enabled by a variety of fabrication methods, involving solution processing[5,6] and vapor deposition,[7] many of which can be performed at low temperatures.[8] Following world record-breaking advances in perovskite-silicon tandem cells, large-scale commercial production has been planned for 2022.[9]

While the efficiencies of "champion cells" have increased rapidly, significant challenges to the commercial development of these devices remain, including long-term stability, reliance on toxic materials, and understanding of the effects of ion motion on the optoelectronic performance.[10,11] The electrical characterization of PSCs using standard photovoltaic (PV) techniques is hampered by showing transients on timescales of several seconds to hours not seen in previous PV technologies. Current–voltage (J–V) measurements (intended to show steady-state performance), which are typically performed at constant sweep rates, are therefore dependent on the bias history of the cell and lead to the *so-called* current–voltage

"hysteresis," as first reported by Snaith *et al.*[12] Habisreutinger *et al.*[13] state that prebiasing is among extrinsic factors that affect the scanned efficiency. These measurements typically proceed first with a preconditioning step in which the cell is held at some constant voltage $V_{pre} > V_{OC}$, for a fixed length of time, followed by a voltage sweep in which the applied voltage is reduced to short-circuit (the reverse scan) and then a sweep back to V_{OC} (the forward scan). Typically, a range of scan rates exhibit hysteresis, meaning there is a marked difference between the forward and reverse current–voltage measurements.[14] Even so-called hysteresis-free cells will show hysteresis if a wide enough range of scan rates and temperatures are investigated.

The use of drift-diffusion (DD) models[15–19] offers a powerful tool to improve understanding of PSCs, guiding further development and providing theoretical insight to address some of the remaining challenges. Following the first observations of current–voltage hysteresis in PSCs, several mechanisms were proposed in the literature.[20,21] Ion migration became the favored candidate due to findings that halide ions were mobile on timescales matching those of hysteresis.[22,23] Drift-diffusion models of electrons and holes are an established technique in semiconductor modeling[24,25] and were used to test theories of ion migration in PSCs by incorporating slow-moving ionic species into the model.[15,16,26] This addition, however, introduces extreme spatial and temporal stiffness to the system, requiring tailored approaches to obtain accurate solutions. Stiff equations are those in which solutions undergo substantial variations over short timescales or over small spatial regions and render many numerical techniques unstable. Temporal stiffness occurs due to the disparity in the timescales of motion of ionic (slow) and electronic (fast) species and spatial stiffness due to carrier accumulation in thin Debye layers (∼1.5 nm) near interfaces, predicted by the high density of ion vacancies in the perovskite.[16] While early numerical approaches to solving the DD equations were not capable of solving for physical parameter sets,[15] Courtier *et al.*[27] and Calado *et al.*[28] have both developed reliable numerical approaches without excessive computation times. In the former case, the resulting finite element scheme has been made publicly available with the release of the open-source PSC simulation software, IonMonger[29] while in the latter it has been released as the open source code Driftfusion.

To avoid the computational difficulties of solving such stiff equations, a different approach was taken by Richardson *et al.*,[16,30] in which matched asymptotic analysis was employed to systematically obtain a simple approximate model [termed the surface polarization model (SPM)], which accurately captures the behavior of the underlying mixed ionic–electronic drift-diffusion model over a large portion of the physically relevant parameter space. In the SPM, ions are decoupled from electronic carriers in the perovskite (meaning the electric potential is determined solely by the ionic charge) and the cell is characterized by the charge density stored within the Debye layer near one of the material interfaces (discussed in more detail in Sec. III). Courtier *et al.* later extended the SPM to explicitly include the transport layers.[17] Although the SPM is not always as accurate as numerical solutions to the full DD model, the simplicity of the SPM provides significant additional insight into the mechanisms underlying PSC behavior. Several other studies have also arrived at simplified models of PSCs that approximate the behavior of the full DD model while offering greater insight, although none of them have been systematically derived from the underlying DD model (as the SPM has). Ravishankar *et al.*[31] developed a similar surface polarization model; however, the capacitance relation used for the ionic Debye layers is not compatible with the DD model and, in particular, results in a non-zero surface charge density at the perovskite/transport layer interfaces when the potential difference across these interfaces is zero. Moia *et al.*[32] obtained an equivalent circuit model comprising an ionically gated transistor-interface, and Bertoluzzi *et al.*[33] provided an analytical model of the band diagrams loosely based on Richardson's surface polarization model.

While all four of these simplified models can be said to approximate the full PSC DD model in certain parameter regimes, there is no report to date in which inverted hysteresis was reproduced by any of these models. In particular, the SPM is compared to full numerical solutions for a parameter set that produces inverted hysteresis in Fig. 1, showing significant error in the approximate model. It is the aim of this work to systematically extend the SPM, by deriving to regimes in which inverted hysteresis is observed.

It should be noted that drift-diffusion is not the only type of model used to investigate PSCs. Alternative device-level models include equivalent circuits (ECs). These aim to replicate the device's current–voltage characteristics by constructing a circuit of standard electronic components.[34] While these models have frequently been employed in the study of PSCs, they suffer from a significant drawback. With some exceptions (notably Bennett *et al.*[35] and Moia *et al.*[32]), these equivalent circuits are not derived from any fundamental physical theory, meaning no meaningful interpretation can be drawn.

B. Inverted hysteresis

A hysteretic current–voltage sweep usually exhibits a greater current output throughout the reverse sweep (from open-circuit to short-circuit) than on the forward sweep (from short-circuit to open-circuit),[12,22] sometimes referred to as normal hysteresis (NH). Some cells, however, have shown a larger current output on the forward sweep than the reverse.[36–40] This has been termed inverted hysteresis (IH).[41,42] While a consensus has not been reached on an exact distinction between NH and IH, the latter includes a higher open-circuit voltage on the forward sweep and/or at least some region of the sweep in which the current output is greater on the forward sweep. Examples of both normal and inverted hysteresis are shown in Fig. 2. Since the phenomenon was first observed, there have been attempts to replicate IH in simulations and models in order to understand the underlying cause, with some success (as discussed below). A consensus on the underlying mechanism has, however, not been reached.

Jacobs *et al.* reproduced IH in numerical drift-diffusion simulations[44] and suggest that preconditioning at voltages much larger than the cell's built-in voltage induced IH due to reverse accumulation of ion vacancies, i.e., positive vacancies accumulate near the ETL, in contrast to normal operating conditions. Although simulations were performed with ions immobilized in some pre-bias configuration, rather than being allowed to evolve in time, a

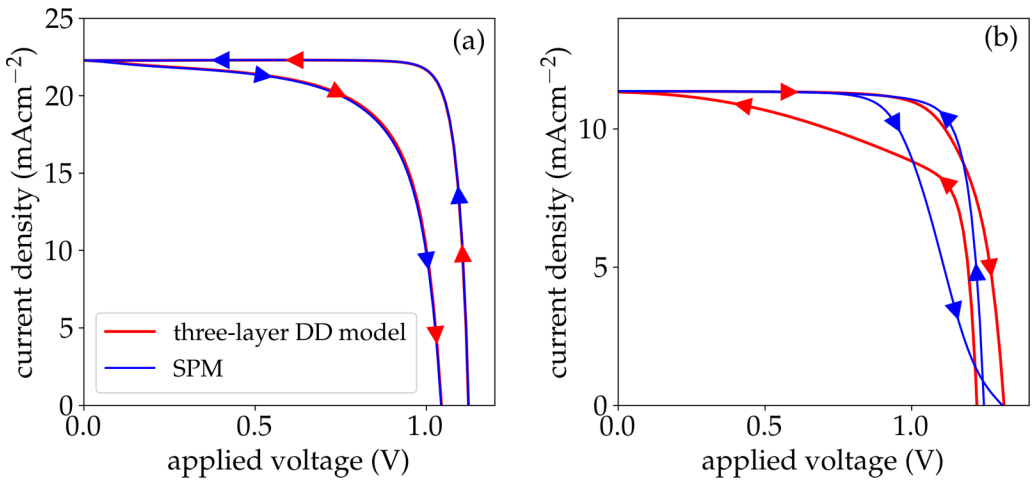

FIG. 1. Validation of the SPM against numerical solutions. Panel (a) shows the current–voltage curve for a 500 mV s^{-1} sweep of the parameter set from Tables 3.2 and 3.3b ofRef. 43 that does not exhibit inverted hysteresis and represents a typical TiO_2/MAPI/spiro-MeOTAD cell while panel (b) shows a 50 mV s^{-1} sweep of a parameter set shown to exhibit strong inverted hysteresis (listed in Table S1 of the supplementary material) and representative of a PCBM/MAPI/NiO_x cell. Red lines are numerical solutions of the full three-layer drift-diffusion model obtained with the PSC simulation software IonMonger[29] and blue lines are numerical solutions of the SPM [Eq. (22) from Ref. 17].

mechanism was proposed. The work presented here builds upon these results by showing this mechanism to be one possible way of inducing IH in a fully dynamic ion migration model.

Shen *et al.*[45] also replicated IH with numerical simulations but drew different conclusions from Jacobs *et al.* as to its underlying causes. In particular, they discussed two possible mechanisms; the first based on band-bending and the second on accumulation of ionic charge in the perovskite bulk. They suggested that highly asymmetrical band alignment between the transport layers and the perovskite causes a significant population of electrons to build up within the perovskite, leading to it becoming n-type, and that any subsequent change to the applied voltage then affects the HTL/perovskite p-n junction, leaving the electric potential uniform over a large region of the cell near the ETL interface. In this region, carrier transport is diffusion-limited, resulting in increased bulk recombination losses. The drift-diffusion model used explicit dynamic coupling of mobile ions to carriers and electric potential.

García-Rodríguez *et al.* used the PSC simulation tool, IonMonger, in conjunction with experimental data to investigate the role of cell architecture on IH.[46] They found that IH can be observed in both p–i–n and n–i–p architectures and that hysteresis typically switches from normal to inverted as the scan rate

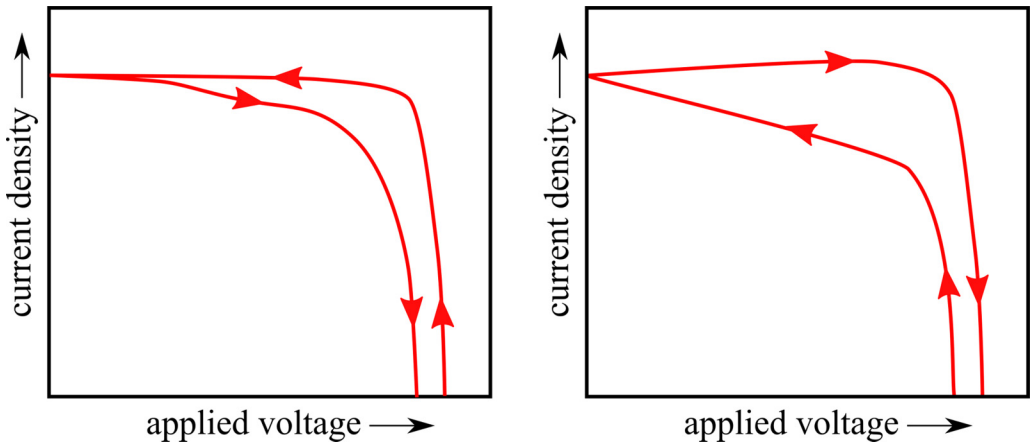

FIG. 2. Schematics of normal (left) and inverted (right) hysteresis.

increases. The scan rates at which maximal normal and inverted hysteresis were shown to be sensitive to the ion vacancy diffusion coefficient, the ion vacancy density, and the nature of the transport layer materials.

Recently, Gonzales *et al.*[47] identified a link between inverted hysteresis and the so-called negative capacitance feature frequently observed in impedance spectra of PSCs.[48] It was found that both phenomena can be well described by the addition of a "chemical inductor" to the equivalent circuit model of a PSC. Despite being able to recreate experimental data, the equivalent circuit models were not derived systematically from the drift-diffusion equations, meaning the physical origin of each circuit element is unclear. Indeed, it was stated that the molecular origin of the chemical inductance has not yet been identified.

Another recent work by Minbashi and Yazdani[49] modified the drift-diffusion model to simulate IH, allowing mobile ions to cross material interfaces. However, two mobile ion species were assumed to have equal mobilities, a scenario shown to be unlikely by Bertoluzzi *et al.*[33] As we shall show here, no additions to the standard drift-diffusion model of PSCs are required to reproduce inverted hysteresis.

Although these studies[44–46] have shown that mixed ionic–electronic drift-diffusion models are capable of exhibiting inverted hysteresis, their numerical simulations do not provide an unambiguous explanation of the underlying mechanism behind this phenomenon. The ambiguity can largely be attributed to the complexity of the mixed ionic–electronic three-layer DD model. As discussed in Sec. I A, simplified models can offer additional insight into the behavior of the full cell but none reported thus far are capable of recreating IH as observed in numerical simulations. In what follows we systematically derive a modified surface polarization model (mSPM), from the mixed ionic–electronic DD model, with the goal of elucidating the mechanisms that underlie inverted hysteresis. We begin, in Sec. II, by stating the familiar mixed ionic–electronic three-layer drift-diffusion (DD) model of a perovskite solar cell. Section III includes a brief description of the standard surface polarization model, as derived in Richardson *et al.*[16] and extended in Courtier *et al.*[17] We show that while the SPM is very accurate for typical parameter sets, it performs poorly for parameter sets exhibiting inverted hysteresis, and this motivates modifications to the assumptions used to derive the SPM. The mSPM and the assumptions on which it is based are discussed in Sec. IV, where solutions are successfully validated against solutions of the full three-layer DD model. In Sec. V, we present further analysis of the problem under external conditions of preconditioning at a fixed voltage and a linear voltage sweep, obtaining a relation between timescales of inverted hysteresis and material parameters. Finally, in Sec. VI, we show that the mSPM reconciles the partial explanations of IH put forward in the literature under a single, complete description and provides a pathway to use IH as a diagnostic tool, which can be used to help guide the design of cells with improved steady-state performance.

II. THE DRIFT-DIFFUSION MODEL

We begin by stating the full drift-diffusion model of the three-layer planar PSC. This model (or minor variations of it) has been widely adopted and shown to accurately reproduce the current–voltage characteristics and impedance response of PSCs.[16–19,29,30,32,50–52] A perovskite absorber layer is sandwiched between an n-type electron transport layer (ETL) and a p-type hole transport layer (HTL). Both n–i–p and p–i–n architectures can be modeled by simply changing the direction of the light. A schematic of the cell is shown in Fig. 3. In each layer, we model transport of each mobile charge species by a conservation equation coupled to a flux equation that is the sum of responses to gradients in electric potential (drift) and number density (diffusion). All charged species are then fully coupled to the electric potential via Poisson's equation. Ion motion is modeled explicitly, allowing for spatial and temporal variation.

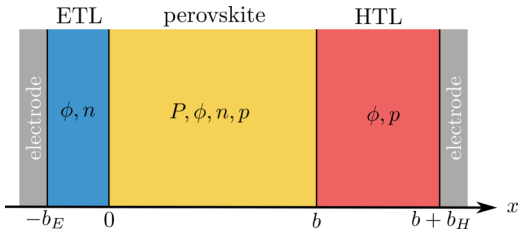

FIG. 3. Schematic of the planar PSC model. The continuum variables modeled in each layer are shown.

A. The perovskite layer

In this layer, we assume three mobile charged species: anion vacancies (P), electrons (n), and holes (p), with fluxes F^P, j^n, and j^p, respectively. The conservation equations and their corresponding fluxes are

$$\frac{\partial P}{\partial t} = -\frac{\partial F^P}{\partial x}, \quad F^P = -D_P\left(\frac{\partial P}{\partial x} + \frac{q}{k_B T} P \frac{\partial \phi}{\partial x}\right), \tag{1}$$

$$\frac{\partial n}{\partial t} = \frac{1}{q}\frac{\partial j^n}{\partial x} + G - R, \quad j^n = qD_n\left(\frac{\partial n}{\partial x} - \frac{q}{k_B T} n \frac{\partial \phi}{\partial x}\right), \tag{2}$$

$$\frac{\partial p}{\partial t} = -\frac{1}{q}\frac{\partial j^p}{\partial x} + G - R, \quad j^p = -qD_p\left(\frac{\partial p}{\partial x} + \frac{q}{k_B T} p \frac{\partial \phi}{\partial x}\right). \tag{3}$$

Here, G and R are the rates of electronic carrier generation and recombination, respectively, forms of which are given in (17)–(21). The three charged species are coupled to the electric potential (ϕ) via Poisson's equation,

$$\frac{\partial^2 \phi}{\partial x^2} = \frac{q}{\varepsilon_p}(N_0 - P + n - p). \tag{4}$$

We have assumed a uniform background density (N_0) of immobile cation vacancies, following the findings of Bertoluzzi *et al.*,[33] which show that cation vacancies are likely either completely immobile or move on much slower timescales than those considered here.

Definitions of material parameter symbols and the values adopted can be found in Table S1 of the supplementary material.

B. The ETL

The electron transport layer is assumed to be highly n-doped. It is assumed that the hole density in this layer is negligible, as are the effects of carrier generation and recombination. In this region, the model, therefore, comprises a single conservation equation for electrons,

$$\frac{\partial n}{\partial t} = \frac{1}{q}\frac{\partial j^n}{\partial x}, \tag{5}$$

coupled to the electron current density

$$j^n = qD_E\left(\frac{\partial n}{\partial x} - \frac{q}{k_{BT}n}\frac{\partial \phi}{\partial x}\right). \tag{6}$$

The electron density is also coupled to the electric potential via Poisson's equation,

$$\frac{\partial^2 \phi}{\partial x^2} = \frac{q}{\varepsilon_E}(n - d_E), \tag{7}$$

where d_E is the effective doping density, equal to the (uniform) density of donor atoms in the lattice. The ETL is assumed to form an Ohmic contact with the metal cathode, leading to the boundary conditions

$$n|_{x=-b_E} = d_E, \quad \phi|_{x=-b_E} = -\frac{V(t) - V_{bi}}{2}, \tag{8}$$

where $V(t)$ is the voltage applied across the cell and

$$V_{bi} = \frac{1}{q}\left(E_c^E - E_v^H\right) - \frac{k_{BT}}{q}\ln\left(\frac{g_c^E g_v^H}{d_E d_H}\right) \tag{9}$$

is the built-in voltage, equal to the difference in the equilibrium quasi-Fermi levels of the transport layers. Here, g_E and g_H refer to the effective density of states for ETL electrons and HTL holes, respectively.

C. The HTL

Similarly, the minority carrier density in the highly p-doped HTL is assumed to be negligible, as are the effects of carrier generation and recombination. The model in this region comprises a single equation for conservation of holes,

$$\frac{\partial p}{\partial t} = \frac{-1}{q}\frac{\partial j^p}{\partial x}, \tag{10}$$

coupled to the hole current density

$$j^p = -qD_H\left(\frac{\partial p}{\partial x} + \frac{q}{k_{BT}p}\frac{\partial \phi}{\partial x}\right). \tag{11}$$

The hole density is coupled to the electric potential via Poisson's equation,

$$\frac{\partial^2 \phi}{\partial x^2} = \frac{q}{\varepsilon_H}(d_H - p), \tag{12}$$

where d_H is the effective doping density, equal to the density of acceptor atoms in the lattice. The HTL is assumed to form an Ohmic contact with the metal anode, leading to the boundary conditions

$$p|_{x=b+b_H} = d_H, \quad \phi|_{x=b+b_H} = \frac{V(t) - V_{bi}}{2}. \tag{13}$$

D. Interface conditions

Electric potential, electric displacement field, and majority carrier QFL are assumed to be continuous across the material interfaces. Similarly, electronic currents are conserved over the interfaces and anion vacancies are confined to the perovskite layer, meaning the ion flux is zero on both interfaces. The resulting continuity conditions are

$$F^P|_{x=0} = 0, \tag{14a}$$

$$j^p|_{x=0} = -qR_l, \tag{14b}$$

$$j^n|_{x=0^-} = j^n|_{x=0^+} - qR_l, \tag{14c}$$

$$\phi|_{x=0^-} = \phi|_{x=0^+}, \tag{14d}$$

$$\varepsilon_E\frac{\partial \phi}{\partial x}|_{x=0^-} = \varepsilon_p\frac{\partial \phi}{\partial x}|_{x=0^+}, \tag{14e}$$

$$k_E n_E|_{x=0^-} = n|_{x=0^+}, \tag{14f}$$

at the ETL interface and

$$F^P|_{x=b} = 0, \tag{15a}$$

$$j^n|_{x=b} = qR_r, \tag{15b}$$

$$j^p|_{x=b^-} - qR_r = j^p|_{x=b^+}, \tag{15c}$$

$$\phi|_{x=b^-} = \phi|_{x=b^+}, \tag{15d}$$

$$\varepsilon_p\frac{\partial \phi}{\partial x}|_{x=b^-} = \varepsilon_H\frac{\partial \phi}{\partial x}|_{x=b^+}, \tag{15e}$$

$$p|_{x=b^-} = k_H p_H|_{x=b^+}. \tag{15f}$$

at the HTL interface. Here, R_l and R_r are the rates of interfacial recombination at the ETL/perovskite and HTL/perovskite interfaces, respectively, in which majority carriers from the transport

layers recombine with minority carriers from the perovskite. The ratios of majority carrier densities on either side of the transport layer interfaces are determined by the band offsets between the adjacent materials,

$$k_E = \frac{g_c}{g_c^E}\exp\left(\frac{E_c^E - E_c}{k_B T}\right), \quad k_H = \frac{g_v}{g_v^H}\exp\left(\frac{E_v - E_v^H}{k_B T}\right). \tag{16}$$

E. Generation and recombination

The rate of carrier generation in the perovskite is assumed to follow the Beer–Lambert law of light absorption for a single wavelength and absorption coefficient,

$$G(x, t) = I_s(t) F_{ph} \alpha\, e^{-\alpha x}, \tag{17}$$

where F_{ph} is the incident photon flux, α is the perovskite absorption coefficient, and $I_s(t)$ is the light intensity. Note that this form of the generation rate assumes the cell has so-called normal architecture (light entering through the ETL). Inverted architectures, in which the light enters through the HTL, can be modeled with the generation rate $G(b - x, t)$. In this cell, bulk recombination is assumed to be dominated by Shockley–Read–Hall (SRH), the rate of which is given by

$$R(n, p) = \frac{np - n_i^2}{\tau_n p + \tau_p n + (\tau_n + \tau_p) n_i}, \tag{18}$$

where τ_n and τ_p are the SRH lifetimes of electrons and holes, respectively. The intrinsic carrier density in the perovskite is defined as

$$n_i^2 = g_c g_v \exp\left(\frac{E_v - E_c}{k_B T}\right). \tag{19}$$

Interfacial recombination is assumed to be dominated by SRH recombination with rates

$$R_l = \frac{np - n_i^2}{\frac{k_E}{v_{n,E}} p + \frac{1}{v_{p,E}} n + \left(\frac{k_E}{v_{n,E}} + \frac{1}{v_{p,E}}\right) n_i}, \tag{20}$$

$$R_r = \frac{np - n_i^2}{\frac{1}{v_{n,H}} p + \frac{k_H}{v_{p,H}} n + \left(\frac{1}{v_{n,H}} + \frac{k_H}{v_{p,H}}\right) n_i}, \tag{21}$$

where v is an SRH recombination velocity with a subscript denoting the carrier species and a superscript denoting the interface at which the recombination is occurring.

III. THE SURFACE POLARIZATION MODEL

While the drift-diffusion (DD) model detailed in Sec. II can be solved numerically,[28,29] deeper physical insight may be gained from approximating the model, in relevant parameter regimes, using asymptotic methods to obtain a simpler, albeit slightly less accurate, model which is more readily analyzed. Many PSCs have

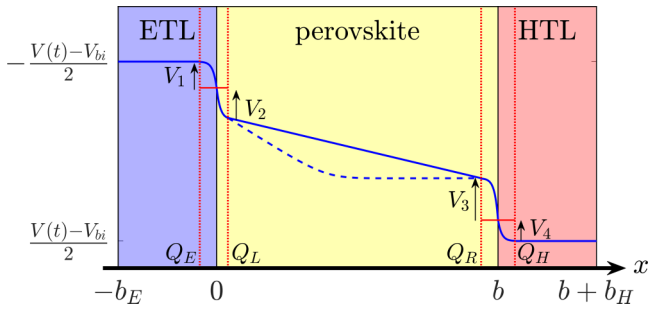

FIG. 4. Electric potential in the SPM. The dashed line shows the adaption to the modified SPM.

physical parameter values for which the DD model is well-approximated by the so-called Surface Polarization Model (SPM) (see Refs. 16, 17, and 30) such that their behavior is accurately captured by this much simpler model. In this section, we give a brief overview of the SPM and discuss its validity for parameter sets that exhibit inverted hysteresis.

The large densities of the dominant mobile charge species in each layer (ion vacancies in the perovskite, electrons in the ETL, holes in the HTL) lead to Debye lengths much smaller than the width of each layer. This motivated Richardson *et al.*[16,30] to apply the method of matched asymptotic expansions to the DD model. In the case of a planar cell with three layers, as depicted in Fig. 4, this leads to a solution with a seven layer structure (see Ref. 17 and Fig. 4) consisting of four narrow boundary layer regions that lie adjacent to the interfaces between the perovskite absorber layer and the transport layers and three bulk regions that lie away from these interfaces. In the boundary layers, there is significant charge accumulation while in the bulk regions there is almost exact charge neutrality. In some cases, the boundary layer charge may be caused by an accumulation of mobile charged species (in which case they may be referred to as Debye layers), whereas in others the depletion of mobile species leaves a net charge caused by immobile background charge (Mott–Schottky type layer).

The systematic derivation of the SPM from the drift-diffusion equations relies on the following five key assumptions:

(i) The Debye length in the perovskite, defined by $L_D = \sqrt{\frac{\varepsilon_p V_T}{qN_0}}$, is small in comparison to the width of the perovskite layer, $\frac{L_D}{b} = \mathcal{O}(10^{-3})$.
(ii) Electron and hole densities in the perovskite layer are very much smaller than that of the mobile ions.
(iii) The timescale for electronic carrier motion is very much faster than that of ion motion in the perovskite.
(iv) The Debye lengths of electrons and holes in their respective transport layers are much smaller than the widths of the transport layers.
(v) The electronic carriers in the transport layers are highly mobile.

Under these assumptions, the electric potential is found to be linear throughout each of the three bulk layers, a consequence of

near total charge neutrality in these regions. Furthermore, each of the boundary layers can be characterized by the surface charge density that it stores (for the four layers, proceeding from left to right, these are denoted by Q_E, Q_L, Q_R, and Q_H, respectively) and the potential drop across it (V_1, V_2, V_3, and V_4, respectively). The charge density in the perovskite boundary layers is dominated by ionic species: anion vacancies accumulate in a thin Debye layer near one interface and deplete from the other, meaning they cannot neutralize the static background ionic defects in this region. Confining these vacancies to the perovskite layer and assuming a constant uniform background density of immobile cation vacancies leads to a condition of net neutrality on the perovskite boundary layers, $Q_L = -Q_R$. Similarly, applying continuity of displacement electric field across the two interfaces leads to the relations $Q_E = -Q_L$ and $Q_H = -Q_R$. This allows Q_E, Q_L, and Q_H to be eliminated in favor of Q_R and results in a single ordinary differential equation (ODE) for Q_R, the charge density stored in the right-hand perovskite boundary layer (Ref. 17),

$$\frac{dQ_R}{dt} = \frac{qN_0D_P}{bk_BT}(V_{bi} - V(t) - V_1 - V_2 - V_3 - V_4), \tag{22}$$

where

$$V_1 = -\mathcal{V}(-\Omega_E\mathcal{Q}_R), \quad V_2 = -\mathcal{V}(-\mathcal{Q}_R), \tag{23}$$

$$V_3 = \mathcal{V}(\mathcal{Q}_R), \quad V_4 = -\mathcal{V}(-\Omega_H\mathcal{Q}_R), \tag{24}$$

are the potential drops over each of the boundary layers, $\mathcal{V}(\mathcal{Q})$ is the non-linear capacitance relation of the boundary layers, defined as the inverse of

$$\mathcal{Q}(\mathcal{V}) = \sqrt{qN_0\varepsilon_pV_T}\,\mathrm{sign}(\mathcal{V})\sqrt{2(e^{\mathcal{V}/V_T} - \mathcal{V}/V_T - 1)}, \tag{25}$$

and $\Omega_E = \frac{\varepsilon_pN_0}{\varepsilon_Ed_E}$ and $\Omega_H = \frac{\varepsilon_pN_0}{\varepsilon_Hd_H}$ are non-dimensional constants that determine how the potential difference across the device is divided between the three layers. Once a time-dependent solution for Q_R has been obtained through numerical solution of the ODE, the current density can be found through solutions of carrier densities in the perovskite bulk on the background electric potential.

Current–voltage curves obtained from the SPM are shown against numerical solutions in Fig. 1. As was shown by Courtier *et al.*,[30] the SPM shows excellent agreement with numerical results for typical parameter sets that do not exhibit IH [Fig. 1(a)] and provides significant insight into the behavior of the complex three-layer drift-diffusion model. However, the model shows poor agreement with numerical solution to the full drift-diffusion model for parameter sets that exhibit IH [Fig. 1(b)] and the understanding of PSCs built upon the SPM needs to be revised in these cases.

IV. THE MODIFIED SURFACE POLARIZATION MODEL

Numerical simulations exhibiting IH typically show a large density of one species of electronic carrier in the perovskite bulk before the sweep begins,[45,46] a feature not usually seen in simulations showing normal hysteresis. Motivated by the link between inverted hysteresis and large carrier densities, we present the modified surface polarization model (mSPM), in which the asymptotic assumptions of the SPM are altered to reflect this carrier population and the systematic analysis of the drift-diffusion equations is repeated with the updated assumptions. In this section, the mSPM is briefly outlined in terms of dimensional variables. The full systematic derivation from the drift-diffusion equations is given in the supplementary material.

The typical ratios of electrons and holes to anion vacancies in the perovskite bulk in steady-state conditions are given by

$$\begin{aligned}\frac{n}{P} &\approx \frac{d_Eg_c}{N_0g_c^E}\exp\left(\frac{E_c^E - E_c - V_1 - V_2}{V_T}\right),\\ \frac{p}{P} &\approx \frac{d_Hg_v}{N_0g_v^H}\exp\left(\frac{E_v - E_v^H - V_3 - V_4}{V_T}\right),\end{aligned} \tag{26}$$

where $V_1 - V_4$ are the potential drops illustrated in Fig. 4 and the parameters in this expression are as defined in Table S1 of the supplementary material. In the standard SPM, the assumption is that both electron and hole densities are sufficiently small that they do not contribute significantly to the net charge density across the perovskite layer (including the Debye layers at its edges). The electron and hole problems thus decouple, at leading order, from the ion problem [reflected in assumption (ii) inSec. III]. As discussed in Sec. III, numerical simulations suggest that this assumption is not justified for parameter sets that exhibit IH due to the presence of significantly larger carrier densities. Here, we shall assume that only one of the electron and hole densities is sufficiently small that it can be neglected from the overall charge density across the perovskite layer and that it is the other charge carrier that has a significant effect on the evolution of the ion density. When preconditioning at voltages larger than V_{bi} (as is common protocol), ion vacancies migrate away from the HTL, leaving a depletion region near the interface.[30] Due to the asymmetry of the boundary layer capacitance relation (Fig. S1 of the supplementary material), a greater potential drop occurs across depletion regions than accumulation regions (Debye layers). This presents holes with a greater extraction barrier than electrons. For this reason, the carrier imbalance is assumed to favor holes over electrons. This manifests itself as an alteration to asymptotic assumption (iii), which now becomes

(i) The hole density in the perovskite bulk is much greater than the electron density, but much less than that of mobile anion vacancies, and the overall contribution to the charge density from holes in the perovskite layer is significant.

The inverse scenario, in which electrons outnumber holes during preconditioning, is discussed in the supplementary material.

In the supplementary material, we generalize the systematic asymptotic approach, adopted in Refs. 16, 17, and 30 to derive the SPM from the DD model, to this new scenario. The results of this analysis show that, while the boundary layers are still characterized by the same capacitance relation (25), the electric potential (ϕ) is no longer approximately linear (i.e., it is no longer true that the electric field is spatially uniform) in the central (bulk) region of the perovskite (i.e., away from the boundary layers on the edges of the perovskite). Instead, ϕ satisfies the following partial differential

equation (PDE) in this region:

$$D_P N_0 \frac{\partial^2 \phi}{\partial x^2} = \frac{d_H g_v}{g_v^H} \exp\left(\frac{V(t) - V_{bi} - 2\phi}{2V_T} + \frac{E_v - E_v^H}{qV_T}\right) \times \frac{\partial}{\partial t}\left(\phi - \frac{V(t)}{2}\right) - \frac{\varepsilon_P V_T}{q}\frac{\partial}{\partial t}\left(\frac{\partial^2 \phi}{\partial x^2}\right), \quad (27a)$$

which couples to the perovskite boundary layer charge densities via the ODEs

$$\frac{dQ_L}{dt} = \frac{qD_P N_0}{V_T}\frac{\partial \phi}{\partial x}|_{x=0^+}, \quad (27b)$$

$$\frac{dQ_R}{dt} = -\frac{qD_P N_0}{V_T}\frac{\partial \phi}{\partial x}|_{x=b^-}, \quad (27c)$$

and satisfies the boundary conditions

$$\phi|_{x=0^+} = -\frac{V(t) + V_{bi}}{2} - V_1 - V_2, \quad (27d)$$

$$\phi|_{x=b-} = \frac{V(t) + V_{bi}}{2} + V_3 + V_4, \quad (27e)$$

where the system is once again completed by the boundary layer potential drops, given as functions of the boundary layer charge densities,

$$V_1 = -\mathcal{V}(\Omega_E Q_L), \quad V_2 = -\mathcal{V}(Q_L), \quad (27f)$$

$$V_3 = \mathcal{V}(Q_R), \quad V_4 = -\mathcal{V}(-\Omega_H Q_L). \quad (27g)$$

Note that, in contrast to the standard SPM model, it is not in general true that $Q_L = -Q_R$; this is because the charge arising from the holes in the perovskite layer is significant and therefore affects the overall charge balance in this layer.

While this system cannot, in general, be solved analytically, the complexity of the full three layer drift-diffusion model has been greatly reduced, retaining only the leading order processes. Further analysis on this system under specific external conditions of interest will be presented inSec. V. Alternatively, this reduced system can easily be solved numerically with a suitable PDE solver as the severe spatial and temporal stiffness of the DD systems is removed by the boundary layer analysis that gives rise to (27b)–(27e), and the assumption that electronic carriers are in a quasi-steady-state [asymptotic assumption (v)].

In order to validate the modified SPM (27), we first consider the example of a current–voltage sweep at 50 mV s^{-1} after the cell has reached steady-state at a preconditioning voltage of 1.4 V. The scan rate was chosen as it shows significant inverted hysteresis for this parameter set, which corresponds to a p-i-n cell with a PCBM/MAPI/NiO_x structure (listed in Table 1 of the supplementary material). Solutions to the modified SPM are compared against numerical solutions to the full three-layer drift-diffusion model obtained using IonMonger.[29]

Figure 5(b) shows the current–voltage curve produced by the modified SPM plotted against a numerical solution of the full three-layer model. The mSPM shows excellent agreement with the numerical solution. In addition to being able to predict the behavior of the J–V hysteresis curves, quantitative properties such as the forward V_{OC}, reverse V_{OC}, and the short-circuit current are

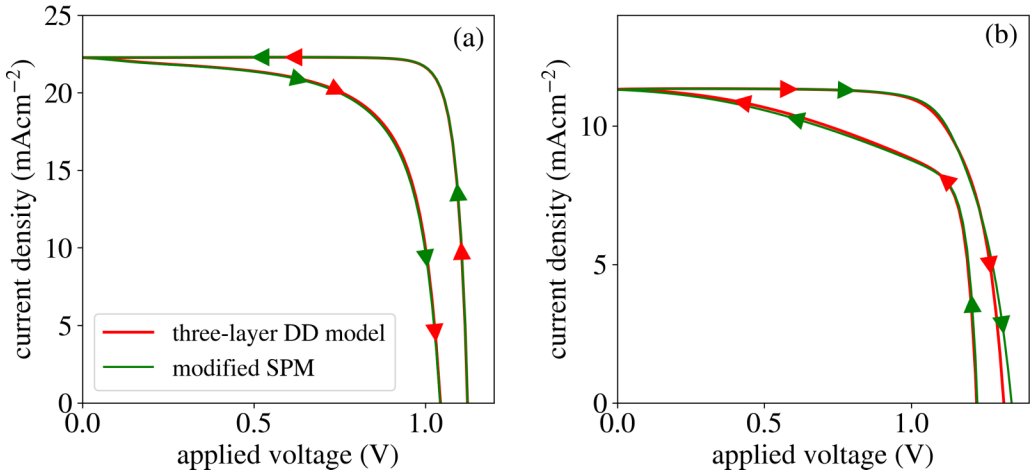

FIG. 5. Validation of the modified SPM against numerical solutions. As in Fig. 1, panel (a) shows the current–voltage curve for a 500 mV s^{-1} sweep of the parameter set from Tables 3.2 and 3.3b ofRef. 43 that does not exhibit inverted hysteresis and represents a typical TiO_2/MAPI/spiro-MeOTAD cell while panel (b) shows a 50 mV s^{-1} sweep of a parameter set shown to exhibit strong inverted hysteresis (listed in Table S1 of the supplementary material) and representative of a PCBM/MAPI/NiO_x cell. Red lines are numerical solutions of the full three-layer drift-diffusion model obtained with the PSC simulation software IonMonger[29] and green lines are numerical solutions of the modified SPM (27).

accurately predicted by the modified SPM, with relative errors of 0.69%, 0.32%, and 1.50%, respectively. However, the standard SPM [shown in Fig. 1(b)] performs poorly, failing to replicate even the qualitative shape of the J–V curve. We also note that the mSPM is capable of reproducing normal hysteresis to the same accuracy as the already-validated SPM [Fig. 5(a)].

Solutions to the electric potential during a reverse voltage sweep are shown in Fig. 6, where they are compared against numerical solutions to the full three-layer DD model. Once again, excellent agreement is seen. While solutions from the standard SPM are not shown, the assumption that the electric potential is linear [i.e., the electric field $E(t)$ is spatially uniform] in the perovskite bulk is clearly not accurate in this case. This confirms that the underlying mechanism of inverted hysteresis that is displayed by this parameter set cannot be explained by the SPM, but requires the additional effects of a large hole population in the perovskite bulk.

The excellent agreement between the modified SPM and numerical solutions is not restricted to this single scan rate, but extends across the entire range of hysteretic scan rates. This is shown in Fig. 7, where hysteresis factor is shown as a function of scan rate as predicted by the three methods of solution. Once again, the modified SPM performs very well, while the standard SPM does not, failing to predict a non-negligible negative hysteresis factor at any scan rate. While the hysteresis factor, defined by

$$\mathrm{HF} = \frac{\int_{V_{\min}}^{V_{\mathrm{OC}}} (J_{\mathrm{rev}} - J_{\mathrm{for}})\, dV}{\int_{V_{\min}}^{V_{\mathrm{OC}}} J_{\mathrm{rev}}\, dV}, \tag{28}$$

obscures much of the information regarding the nature of the hysteresis[13,42] and should not be used as the only measure of hysteresis, it does offer convincing evidence that the modified SPM can be considered accurate across a broad range of scan rates.

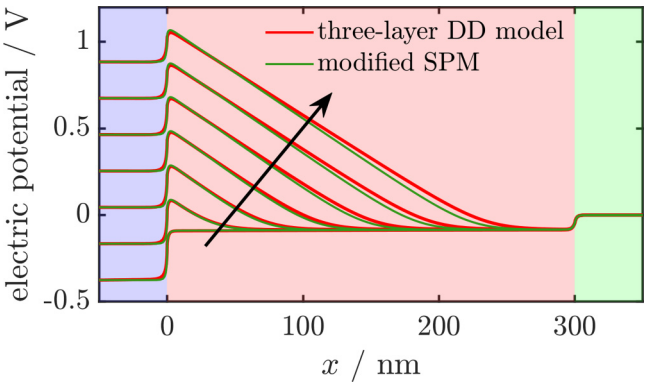

FIG. 6. Solutions of the electric potential during the 50 mV s^{-1} reverse sweep of a PCBM/MAPI/NiO$_x$ parameter set that exhibits strong inverted hysteresis (see Table 1 of the supplementary material). Red lines correspond to numerical solutions from IonMonger and green lines to numerical solutions of the modified SPM (27). The arrow shows the direction of increasing time. Note that here electric potential has been shifted by a time-dependent function such that the right-hand boundary condition is now $\phi|_{x=b+b_H} = 0$ in order to more clearly show the behavior of the solution.

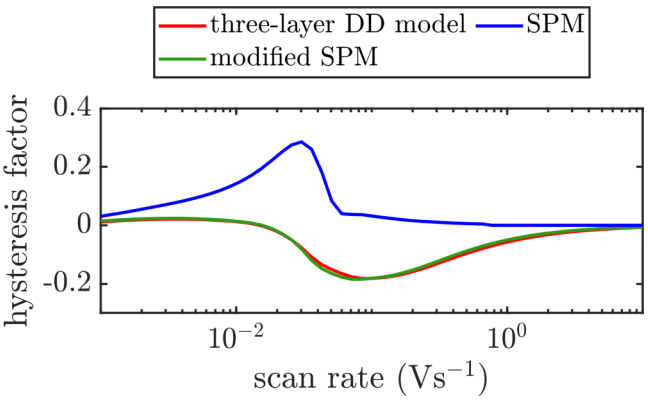

FIG. 7. Hysteresis factor (28) as a function of scan rate from three methods of solution. The red line shows full numerical solutions using IonMonger, the blue shows solutions of the SPM, and the green shows the modified SPM.

V. ANALYSIS

The modified SPM is a much simpler model of a PSC than the full DD model and predicts its behavior from a single non-stiff PDE for the electric potential ($\phi(x, t)$) in the perovskite bulk coupled to two ODEs for the charge densities [$Q_L(t)$ and $Q_R(t)$] in the boundary layers. Furthermore, numerical solutions to the modified SPM show close agreement (in the relevant regimes) to those of the full DD model. In this section, we further analyze the modified SPM to obtain a traveling wave solution, which accurately describes the reverse sweep of a hysteresis experiment and can be used to explain the phenomenon of inverted hysteresis. Standard procedure for these measurements is to precondition the cell at some voltage $V^{\mathrm{pre}} > V_{OC}$ until steady-state is reached, then linearly sweep the applied voltage to short-circuit and back at some fixed rate.[36,41,45] This motivates us to look for a solution that starts from steady-state at $V = V^{\mathrm{pre}}$ and then evolves in response to a linearly decreasing applied voltage.

A. Preconditioning

To investigate the behavior of the mSPM during the preconditioning stage, we look for steady-state solutions of the modified SPM at some applied voltage V^{pre}. Steady-state is enforced by setting all time derivatives in the governing equations (27a)–(27c) to be equal to zero. Under these conditions, the electric potential solution in the perovskite bulk is flat (i.e., independent of x),

$$\phi^{\mathrm{pre}} = \frac{V^{\mathrm{pre}} - V_{bi}}{2} + V_3^{\mathrm{pre}} + V_4^{\mathrm{pre}}, \tag{29}$$

where $V_{1,\ldots,4}^{\mathrm{pre}}$ are the four boundary layer potential drops, determined by the boundary layer charge densities (Q_L^{pre}, Q_R^{pre}) according to (27f) and (27g). As no potential difference occurs across any of the bulk regions, the sum of the boundary layer potential drops must equal the total potential across the cell,

$$V_1^{\mathrm{pre}} + V_2^{\mathrm{pre}} + V_3^{\mathrm{pre}} + V_4^{\mathrm{pre}} = V_{bi} - V^{\mathrm{pre}}. \tag{30}$$

A third constraint is required to completely solve the system, provided by a statement of conservation of ionic charge. While the drift-diffusion equations require the total ionic charge in the perovskite to be constant, we also require ionic net neutrality, a condition usually supplied by initial conditions for the problem. This condition of ionic charge conservation and neutrality takes the form

$$\int_0^b (P - N_0)\, dx = 0. \tag{31}$$

This third constraint shows that (unlike in the standard SPM) the ionic charge densities stored in the perovskite Debye layer and depletion region are not necessarily equal and opposite and depend on the preconditioning voltage,

$$Q_L^{\text{pre}} + Q_R^{\text{pre}} = q d_H k_H b \exp\left(\frac{V^{\text{pre}} - V_{bi} + V_1^{\text{pre}} + V_2^{\text{pre}}}{V_T}\right). \tag{32}$$

This is caused by large hole densities flooding the perovskite when the preconditioning voltage is high. This accumulation of positive charge in the bulk forces anion vacancies to move from the bulk into the boundary layers, disturbing their net neutrality. Both the anion vacancy density and the hole density are uniform in the perovskite bulk being given by the expressions

$$P^{\text{pre}} = N_0 - \frac{1}{bq}\left(Q_L^{\text{pre}} + Q_R^{\text{pre}}\right), \tag{33}$$

$$p^{\text{pre}} = \frac{1}{bq}\left(Q_L^{\text{pre}} + Q_R^{\text{pre}}\right). \tag{34}$$

B. Analysis of the reverse sweep

The preconditioning step results in the cell reaching a steady state in which a large hole population in the perovskite bulk pushes ion vacancies from the bulk into the boundary layers. Here, the voltage scan from this preconditioning toward short-circuit conditions is considered. When a change occurs in the applied voltage, the electric field takes some finite time to permeate through the entire perovskite layer, seen in the time dependence of (27). To analyze the motion of the electric field through the device, we nondimensionalize as follows:

$$x^* = \frac{x}{b}, \quad t^* = \frac{t}{\tau_{\text{ion}}}, \phi^* = \frac{\phi}{V_T}, \tag{35a}$$

$$\mathcal{Q}_{L,R}^* = \frac{Q_{L,R}}{\sqrt{qN_0\varepsilon_p V_T}}, \mathcal{V}_{1,\ldots,4}^* = \frac{V_{1,\ldots,4}}{V_T}. \tag{35b}$$

Here, τ_{ion}, the typical timescale of ion vacancy motion, is defined by

$$\tau_{\text{ion}} = \frac{b}{D_P}\sqrt{\frac{V_T\varepsilon_p}{qN_0}}. \tag{36}$$

Henceforth, the asterisk, denoting a dimensionless variable, is dropped as all quantities in what follows (unless otherwise stated) are dimensionless. In addition, we define φ, the shifted electric potential, by

$$\varphi = \phi - \phi^{\text{pre}} - \frac{\Phi(t) - \Phi^{\text{pre}}}{2}, \tag{37}$$

where $\Phi(t) = V(t)/V_T$ denotes the dimensionless applied voltage, and the superscript "pre" denotes the quantity from the steady-state preconditioning solution. Note that ϕ^{pre} is the spatially independent electric potential in the perovskite bulk from the steady-state reached during preconditioning.

After applying these scaling factors, the dimensionless governing equations of the modified SPM (27) become

$$\frac{d\mathcal{Q}_L}{dt} = \frac{\partial\varphi}{\partial x}\Big|_{x=0}, \tag{38a}$$

$$m_p\lambda\alpha\, e^{-\varphi}\frac{\partial\varphi}{\partial t} - \lambda\frac{\partial}{\partial t}\left(\frac{\partial^2\varphi}{\partial x^2}\right) = \frac{\partial^2\varphi}{\partial x^2}, \tag{38b}$$

$$\frac{d\mathcal{Q}_R}{dt} = -\frac{\partial\varphi}{\partial x}\Big|_{x=1}, \tag{38c}$$

and satisfy the boundary conditions

$$\varphi|_{x=0} = \psi_0(t), \quad \varphi|_{x=1} = \psi_1(t), \tag{38d}$$

where

$$\psi_0(t) = -\Phi(t) + \Phi_{bi} - \mathcal{V}_1 - \mathcal{V}_2 - \mathcal{V}_3^{\text{pre}} - \mathcal{V}_4^{\text{pre}}, \tag{38e}$$

$$\psi_1(t) = \mathcal{V}_3 + \mathcal{V}_4 - \mathcal{V}_3^{\text{pre}} - \mathcal{V}_4^{\text{pre}}. \tag{38f}$$

The three dimensionless constants appearing in Eq. (38b) are defined as follows:

$$\lambda = \frac{1}{b}\sqrt{\frac{V_T\varepsilon_p}{qN_0}}, \tag{39a}$$

$$m_p = \frac{d_H b^2 q g_v}{V_T\varepsilon_p g_v^H}\exp\left(\frac{E_v - E_v^H}{qV_T}\right), \tag{39b}$$

$$\alpha = \exp\left(-\frac{V_3^{\text{pre}} + V_4^{\text{pre}}}{V_T}\right). \tag{39c}$$

Here, λ corresponds to the ratio of the Debye length to the width of the perovskite layer, m_p to the typical ratio of holes to ion vacancies, and α is a factor that measures how easily holes can enter the perovskite from the HTL during the preconditioning step. *The ratio of holes to ion vacancies, m_p, is of particular importance as it is this that determines the susceptibility of the cell to inverted hysteresis in terms of material parameters.*

The cell is in steady-state at the preconditioning voltage for times $t < 0$. The commencement of the voltage sweep, which starts

at $t = 0$, perturbs the cell from its steady-state. The steady-state preconditioning solutions found in Sec. V A are used to determine initial conditions for (38) and, in particular, lead to the conditions $\psi_0(0) = \psi_1(0) = 0$.

From the boundary conditions (38e) and (38f), it is clear that a decrease in the applied voltage will manifest itself as an increase in φ at the left-hand boundary of the perovskite bulk, inducing a positive electric field in this region. Due to the nonlinear diffusion of φ, this electric field takes a finite time to permeate through the perovskite layer. Until the field reaches the right-hand boundary, $\mathcal{Q}_R$ (and consequently $\mathcal{V}_3$ and $\mathcal{V}_4$) remain constant and equal to their values in the preconditioning step. During this period, the right-hand boundary condition on φ is, therefore, $\psi_1(t) = 0$.

1. Traveling wave solutions

Numerical solutions to this problem show the solution split into three regions: two large linear regions connected by a thin inner region that migrates from left to right across the perovskite layer, as shown in Fig. 8. Motivated by these results, we investigate this solution using matched asymptotic expansions. In the two outer regions, $\frac{\partial^2 \phi}{\partial x^2}$ is small such that the left- and right-hand outer solutions are, in leading order,

$$\varphi^L = \psi_0(t) - E^L(t)x, \tag{40}$$

$$\varphi^R = \psi_1(t) - E^R(t)(x - 1), \tag{41}$$

respectively, where E^L and E^R are the electric field strengths in these regions, which are determined by matching to the inner solution. Furthermore, numerical solutions imply that the electric potential in the right-hand outer solution remains flat, which suggests that $E^R(t) = 0$.

We assume that the inner region is of width ϵ, where $\epsilon \ll 1$ and will be determined as part of the solution, and that it migrates

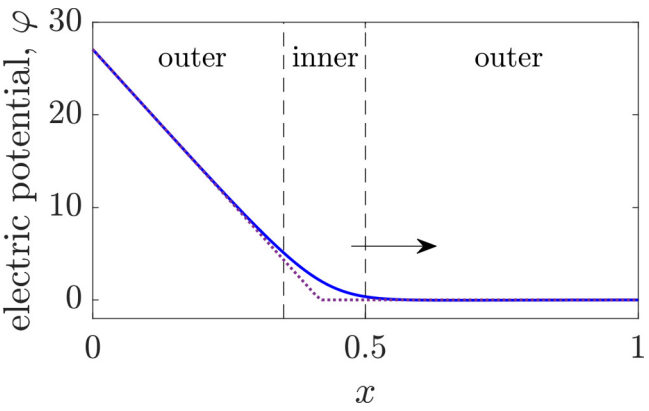

FIG. 8. The three regions of the solution to (38b) during the reverse sweep. The blue line is a numerical solution to (38b) and the purple dotted line shows an extrapolation of the two outer solutions into the boundary region. The arrow shows the direction of motion of the inner region.

at a speed c, starting from the left-hand boundary ($x = 0$) at $t = 0$. This motivates us to expand Eq. (38b) about the point $x = ct$ (the location of the inner layer) and write the problem in the stretched traveling wave coordinates,

$$\hat{x} = \frac{x - ct}{\epsilon}, \quad \hat{t} = t. \tag{42}$$

Under this transformation, (38b) becomes

$$\frac{\epsilon}{\lambda c}\frac{\partial^2 \varphi}{\partial \hat{x}^2} = \frac{m_p \alpha \epsilon^3}{c} e^{-\varphi}\frac{\partial \varphi}{\partial \hat{t}} - m_p \alpha \epsilon^2 e^{-\varphi}\frac{\partial \varphi}{\partial \hat{x}} - \frac{\epsilon}{c}\frac{\partial}{\partial \hat{t}}\left(\frac{\partial^2 \varphi}{\partial \hat{x}^2}\right) + \frac{\partial^3 \varphi}{\partial \hat{x}^3}. \tag{43}$$

A suitable choice for the boundary layer width is

$$\epsilon = (m_p \alpha)^{-\frac{1}{2}}, \tag{44}$$

such that (43) can be rewritten as

$$\beta\frac{\partial^2 \varphi}{\partial \hat{x}^2} = \frac{\epsilon}{c} e^{-\varphi}\frac{\partial \varphi}{\partial \hat{t}} - e^{-\varphi}\frac{\partial \varphi}{\partial \hat{x}} - \frac{\epsilon}{c}\frac{\partial}{\partial \hat{t}}\left(\frac{\partial^2 \varphi}{\partial \hat{x}^2}\right) + \frac{\partial^3 \varphi}{\partial \hat{x}^3}, \tag{45}$$

where the parameter β is defined by

$$\beta = \frac{\epsilon}{\lambda c}. \tag{46}$$

Since we implicitly assume that $\epsilon \ll c$, both terms containing a time derivative can be neglected, to give the leading order balance in the inner region

$$\frac{d^3 \varphi}{d\hat{x}^3} - \beta\frac{d^2 \varphi}{d\hat{x}^2} - e^{-\varphi}\frac{d\varphi}{d\hat{x}} = 0. \tag{47}$$

In order to match the solution to the right-hand outer solution, we impose the matching condition $\varphi \to 0$ as $\hat{x} \to \infty$. We integrate (47) once and apply this condition to obtain

$$\frac{d^2 \varphi}{d\hat{x}^2} - \beta\frac{d\varphi}{d\hat{x}} + e^{-\varphi} - 1 = 0. \tag{48}$$

We reduce the order of this problem by introducing a second variable (u),

$$u = \frac{d\varphi}{d\hat{x}}, \quad \frac{du}{d\hat{x}} = \beta u - e^{-\varphi} + 1, \tag{49}$$

and turn to a phase plane (Fig. 9) to visualize solutions. The phase plane is a mathematical tool in which the direction of the derivative of (φ, u) with respect to $\hat{x}$ is drawn as an arrow for each point in the (φ, u) plane. Thus, each arrow points in the direction that the solution to (49) would take, were it given the origin of the arrow as an initial condition.

Notably, all phase planes with $\beta > 0$ exhibit the same qualitative features and show two solutions that satisfy the right-hand

matching condition by terminating at the critical point $(\varphi, u) = (0, 0)$. However, the solution in the second quadrant (green curve in Fig. 9) becomes infinitely negative as $\hat{x} \to -\infty$, and so is clearly inconsistent with the left-hand boundary condition (which is positive for a reverse sweep). We, therefore, adopt the solution in the fourth quadrant (blue curve in Fig. 9). Matching to the left-hand outer solution and applying the boundary condition at $x = 0$ will identify β (and, therefore, c also) as a function of the sweep rate. As seen in the phase plane, the gradient u tends toward a finite constant as $\hat{x} \to -\infty$, identifiable from (49) as $u \to \frac{-1}{\beta}$. Thus far, we have not defined the point $x = ct$ and, therefore, have the freedom to define it as the point at which the left-hand outer solution becomes zero, i.e., $\varphi^L|_{x=ct} = 0$. The far-field behavior of the inner solution on the left-hand side is, therefore, $\varphi \sim \frac{-\hat{x}}{\beta}$ as $\hat{x} \to -\infty$. On rewriting $\hat{x}$ in terms of outer coordinates and matching to the left-hand outer region, we see that the left-hand outer solution is, in leading order,

$$\varphi^L = \frac{1}{\epsilon\beta}(ct - x) \quad \text{for} \quad x < ct. \tag{50}$$

On imposing the boundary condition (38d) on $x = 0$, and referring back to the definitions of ϵ and β [(44) and (46)], we obtain the following expression for the wavespeed:

$$c = \frac{\psi_0(t)\epsilon\beta}{t} = \sqrt{\frac{\psi_0(t)}{m_p\alpha\lambda t}}. \tag{51}$$

We also note that the leading order outer electric field is given by

$$E^L(t) = \frac{1}{\epsilon\beta} = m_p\alpha c\lambda. \tag{52}$$

It remains to relate the function $\psi_0(t)$ to the applied voltage and to redimensionalize to obtain the wavespeed as a function of the material parameters.

The boundary condition (38e) contains a linear component corresponding to the applied voltage and two highly nonlinear components corresponding to the boundary layer potential drops and begins from $\psi_0(0) = 0$. When the sweep rate is large, the sweep will finish before the boundary layers can discharge due to the slow nature of the ion motion, meaning ψ_0 is dominated by the change in applied voltage and can be approximated by

$$\psi_0(t) \approx -\frac{d\Phi}{dt}t, \tag{53}$$

where $\frac{d\Phi}{dt}$ is the (constant) sweep rate. At slower scan rates, the boundary layers have time to discharge but numerical simulations show that the wavefront typically crosses the layer faster than timescales of boundary layer discharge. For this reason, (53) is a valid approximation for slow scan rates during the time before the wavefront has crossed the layer. Under this approximation, the wavespeed (51) becomes a constant,

$$c = \sqrt{-\frac{d\Phi}{dt}\frac{1}{m_p\alpha\lambda}}. \tag{54}$$

After reapplying the scalings in (35), we obtain the dimensional speed of the wavefront in terms of material parameters,

$$c_{\text{dim.}} = \sqrt{\frac{-D_P N_0 g_\nu^H}{V_T d_H g_\nu}\frac{dV}{dt}}\exp\left(\frac{V_3^{\text{pre}} + V_4^{\text{pre}} + E_\nu^H - E_\nu}{2V_T}\right). \tag{55}$$

This approximation for the wavefront speed displays excellent agreement with the numerical solutions of the full three-layer drift-diffusion model obtained from IonMonger, as shown in Fig. 10.

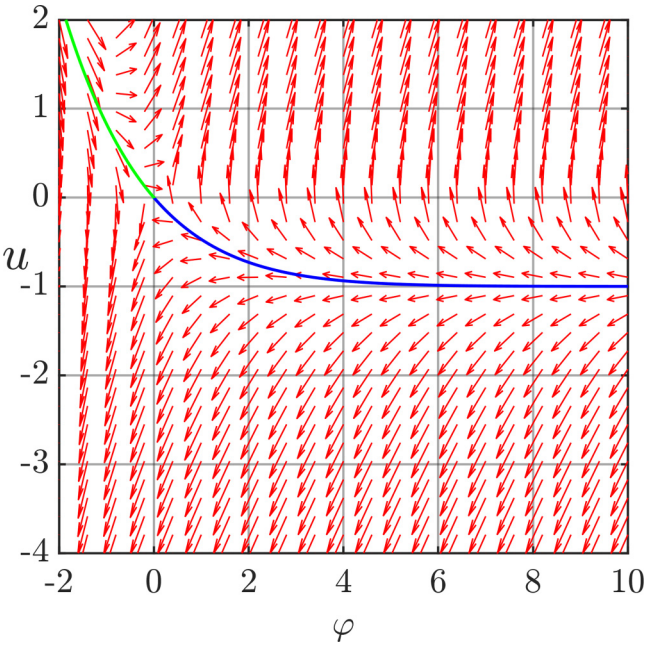

FIG. 9. Phase plane of the inner problem (49) where $\beta = 1$. Red arrows show the direction of the derivative of the vector (φ, u) with respect to $\hat{x}$, as given by (49). Solid lines show the two solutions that meet the right-hand matching condition. Only the blue line can meet the left-hand matching condition.

C. The effect of recombination on hysteresis

The traveling wave solution to the bulk electric potential problem divides the perovskite bulk into two regions: (I) ahead of the wavefront ($x > ct$), the electric field strength is negligible, and (II) behind the wavefront ($x < ct$), the electric field strength is strong and positive. In the first region, carrier distributions remain at their (approximately uniform) steady-state distributions found during preconditioning with a large density of holes [given by (34)] and a much smaller density of electrons, as shown in Fig. 11. Once the wavefront has passed through a region, however the

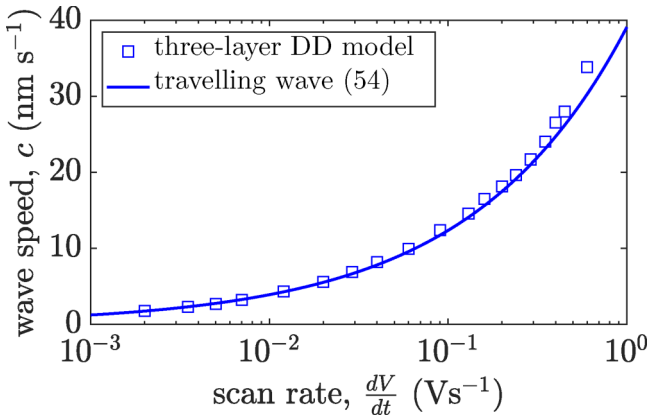

FIG. 10. Comparison between the traveling wavefront solution and the full three-layer DD model for wavefront speed across a range of experimentally relevant scan rates. Squares are data from numerical solutions using IonMonger and the solid line is the traveling wavefront solution (55).

strong electric field quickly removes carriers, pushing them toward their respective transport layers for extraction. Both hole and electron densities are, therefore, small in this region.

The effect on the observed hysteresis of this wavefront is determined by the recombination parameters. Here, we consider three distinct regimes: (i) hole-limited SRH recombination in the bulk, (ii) interfacial SRH recombination only, and (iii) a combination of the first and second types.

(i) Hole-limited bulk recombination: When recombination in the perovskite bulk is strongly hole-limited ($\tau_p \gg \tau_n$), current losses occur in the hole-rich region ahead of the wavefront but not in the region behind, as shown in Fig. 11, meaning performance is inhibited at the beginning of the sweep but recovers as the wavefront reaches the HTL interface, and the cell approaches short-circuit. In this scenario, $J_{rev} < J_{for}$ for most or all of the power-generating region, giving a negative hysteresis factor (28).

(ii) Interfacial recombination only: When bulk recombination is neglected and interfacial recombination considered, the behavior of the electric potential wavefront is unchanged but the resulting effect on the current density is significantly different. As the wavefront traverses the perovskite layer, generated carriers are no longer lost to bulk recombination but instead eventually drift or diffuse toward their respective transport layers. Therefore, during this period, current output is not inhibited by the wavefront. Once the wavefront has crossed the entire layer, however, the (now-uniform) electric field in the perovskite bulk will eventually switch sign, driving carriers toward the wrong transport layers, resulting in large surface recombination losses at the interfaces. Current density is, therefore, inhibited only after the wavefront has completed its journey, resulting in a positive hysteresis factor ($J_{rev} > J_{for}$).

(iii) Interfacial and bulk recombination: Introducing a combination of bulk and interfacial recombination leads to mixed normal and inverted hysteresis, as shown in Fig. 12. At high scan rates, most or all of the sweep occurs before the wavefront has traversed the perovskite layer, leading to the bulk losses described in **(i)** that cause inverted hysteresis. At lower scan rates, however, most of the scan occurs after the wavefront has traversed the layer, causing the interfacial losses described in **(ii)** that cause normal hysteresis. This switchover from normal to inverted hysteresis as the scan rate becomes higher has been observed experimentally.[46,47]

The scan rate at which the hysteresis switches from positive to negative can be related to material parameters using the wavefront analysis performed in Sec. V B. This scan rate is that at which the wavefront crosses the perovskite layer in the same time as which is

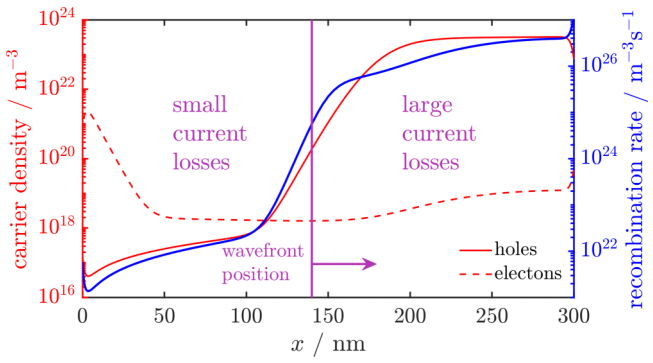

FIG. 11. Carrier densities (red) and bulk recombination rate (blue) in the perovskite layer at a point during the reverse sweep as calculated by IonMonger. Recombination parameters determine that bulk recombination is strongly hole-limited and interfacial recombination is neglected. The region of large current losses occupies the entire layer at the beginning of the sweep but recedes, resulting in the recovery of current density throughout the sweep symptomatic of IH.

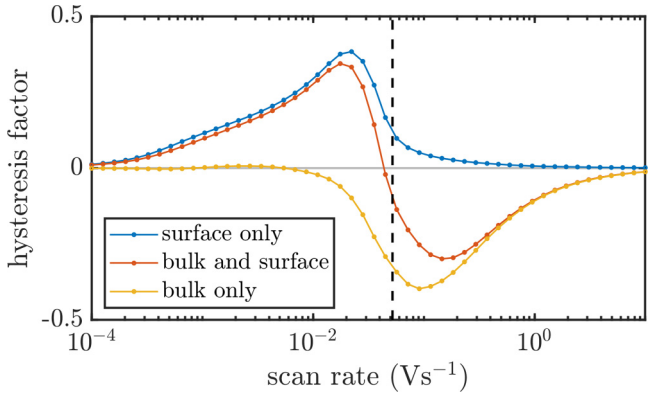

FIG. 12. Hysteresis factor as a function of scan rate under different recombination regimes. All simulations were performed in IonMonger using the parameter set in Table S1 with the recombination parameters in Table S2 of the supplementary material following preconditioning at 1.4 V. All three simulations exhibit the same wavefront behavior. The black dashed line is the scan rate, given by Eq. (56), at which normal hysteresis is predicted to switch to inverted hysteresis by the wavefront analysis.

taken for the reverse sweep such that the bulk recombination losses occur on the reverse sweep and surface recombination losses on the forward sweep. Using the wavefront speed (55), this scan rate is found to be

$$\left|\frac{dV}{dt}\right| = \frac{D_P N_0 V_{\text{pre}}^2 g_v^H}{V_T b^2 d_H g_v} \exp\left(\frac{V_3^{\text{pre}} + V_4^{\text{pre}} + E_v^H - E_v}{V_T}\right), \tag{56}$$

where V_{pre} is the voltage from which the sweep begins. At lower scan rates, the wavefront completes its journey before the cell reaches short-circuit, meaning most of the sweep is spent in the regime in which surface recombination, and therefore normal hysteresis, dominate. Similarly, at larger scan rates, the wavefront does not complete its journey until after the cell reaches short-circuit, meaning more time is spent in the region in which bulk recombination, and therefore, inverted hysteresis, dominates. This prediction of the switchover scan rate is compared against solutions of the full DD model in Fig. 12.

Whereas the timescales of hysteresis (normal or inverted) are determined by material parameters, the sign and magnitude of the hysteresis can signify the location and severity of the dominant recombination mechanism in the cell. A cell that shows inverted hysteresis across the full range of hysteretic scan rates is dominated by hole-limited bulk recombination, whereas the presence of a positive peak at a lower scan rate than the negative peak (as measured experimentally by Garcia-Rodriguez *et al.*[46]) indicates interfacial recombination where the relative sizes of the two peaks are determined by the relative magnitudes of the two recombination sources.

VI. CONCLUSIONS

In summary, an asymptotic analysis of the drift-diffusion model of a three-layer planar PSC has been used to show that a high density of one of the carriers inside the perovskite layer after preconditioning results in a wavefront (in electric potential) propagating across the perovskite layer during the reverse voltage sweep. The electric field propagates with this wavefront and, therefore, takes some time to permeate the entire perovskite layer, with the region ahead of the wavefront being diffusion-limited. If bulk recombination is strongly limited by the majority carrier in the perovskite, significant current losses occur in the region ahead of the front (where the electric field is weak and there is a high density of majority carriers) and it is not until the wavefront has crossed the entire perovskite layer that the losses are reduced to a low level. This leads to the observation of inverted hysteresis since current losses are higher on the reverse sweep than the forward sweep that follows it.

This description of IH unifies the mechanisms proposed in the literature based upon numerical simulations of the DD model.[44–46] However, none of the explanations offered in these works provide a comprehensive explanation of the phenomenon.

Plots of carrier density and recombination rate by García-Rodríguez *et al.*[46] exhibit the large variation between the regions in front of and behind the wavefront only for parameter sets that display inverted hysteresis but the movement of the wavefront across the layer or the conditions necessary for it to appear were not discussed. Similarly, the large preconditioning voltage found to be necessary by Jacobs *et al.*[44] is one way of inducing large hole populations in the perovskite due to the asymmetric extraction barriers caused by the capacitance relations of the boundary layers but, once again, the wavefront was not identified (perhaps due to the limitations of the model used). Unlike these works, Shen *et al.*[45] correctly identified the existence of a diffusion-limited region during sweeps that show inverted hysteresis as a result of significant accumulated charge in the bulk. This work has been built upon here by analysis of the evolution of this diffusion-limited region, linking timescales of inverted hysteresis to macroscopic material parameters.

It has also been shown that, in principle, IH could be seen as a result of either electrons outnumbering holes or holes outnumbering electrons. However, preconditioning at large voltages presents a greater extraction barrier to holes than electrons, due to the asymmetry of the boundary layer capacitance relation, and the conclusions of Stranks *et al.*[53] suggest that SRH recombination in perovskites is typically hole-limited. Both of which suggest that holes outnumbering electrons is a far more likely scenario when inverted hysteresis is observed. The conditions that influence this are summarized in Sec. VI A.

A. Inverted hysteresis as a diagnostic tool

In recent years, interest in current–voltage hysteresis has begun to wane in the PSC community, due to its focus on pushing the PCE of "champion" cells and the mistaken belief that hysteresis is only seen in poor cells[54] (for example, Refs. 55–57 report high performance cells that still exhibit hysteresis). However, in order to continue to increase the efficiency and stability of average cells, and the consistency across many batches, it is vital to develop our understanding of the internal mechanisms of devices.

The results of the modified SPM, therefore, suggest that observation of inverted hysteresis offers a glimpse into the limiting factor of a cell's performance and a chance to improve a cell's steady-state efficiency. The dimensionless constants that determine the influence of electrons and holes, respectively, on the electric potential in the perovskite (usually thought to be negligibly small in previous models) are defined in terms of dimensional material parameters as

$$m_n = \frac{d_E b^2 q g_c}{V_T \varepsilon_p g_c^E} \exp\left(\frac{E_c^E - E_c}{k_B T}\right), \tag{57a}$$

$$m_p = \frac{d_H b^2 q g_v}{V_T \varepsilon_p g_v^H} \exp\left(\frac{E_v - E_v^H}{k_B T}\right). \tag{57b}$$

The exponential dependence of these constants on transport layer band offsets suggests that these are the material properties to which inverted hysteresis (and the large carrier densities of which it is symptomatic) is most sensitive. Therefore, if inverted hysteresis is still observed when the preconditioning voltage is decreased, approaching V_{OC}, it is likely that one of the transport layer band offsets is insufficient for efficient carrier extraction and the cell could be improved by substitution of an alternative transport layer

material that forms a greater band offset with the perovskite. Furthermore, the magnitude of inverted hysteresis has been shown to indicate the level of bulk recombination occurring in the cell, with the magnitude of normal hysteresis indicating the corresponding level of surface recombination occurring at the interfaces. Together, these observations from the modified SPM provide a pathway to improve the stabilized efficiency of a cell that displays inverted hysteresis.

SUPPLEMENTARY MATERIAL

See the supplementary material for the material parameter values obtained for a PCBM/MAPI/NiO_x cell from which Figs. 1(b), 5(b), 6, 7, 10, 11, and 12 were generated; a derivation of the modified surface polarization model from the drift-diffusion model; and discussion of the model for the inverse case, in which electrons are the majority carrier in the perovskite.

AUTHOR DECLARATIONS

Conflict of Interest

The authors have no conflicts to disclose.

Author Contributions

Will Clarke: Conceptualization (equal); Formal analysis (equal); Investigation (equal); Software (lead); Visualization (equal); Validation (equal); Writing – original draft (lead); Writing – review & editing (equal). **Matthew V. Cowley:** Conceptualization (equal); Investigation (equal); Writing – review & editing (supporting). **Matthew Wolf:** Conceptualization (equal); Supervision (supporting); Writing – review & editing (equal). **Petra Cameron:** Writing – review & editing (equal). **Alison Walker:** Conceptualization (equal); Supervision (supporting); Writing – review & editing (equal). **Giles Richardson:** Conceptualization (equal); Formal analysis (equal); Supervision (equal); Visualization (supporting); Writing – original draft (supporting); Writing – review & editing (equal).

DATA AVAILABILITY

The data that support the findings of this study are available within the article and its supplementary material.

REFERENCES

[1]J. J. Yoo, G. Seo, M. R. Chua, T. G. Park, Y. Lu, F. Rotermund, Y.-K. Kim, C. S. Moon, N. J. Jeon, J.-P. Correa-Baena, V. Bulović, S. S. Shin, M. G. Bawendi, and J. Seo, "Efficient perovskite solar cells via improved carrier management," Nature **590**, 587–593 (2021).
[2]H.-S. Kim, C.-R. Lee, J.-H. Im, K.-B. Lee, T. Moehl, A. Marchioro, S.-J. Moon, R. Humphry-Baker, J.-H. Yum, J. E. Moser, M. Grätzel, and Nam-Gyu Park, "Lead iodide perovskite sensitized all-solid-state submicron thin film mesoscopic solar cell with efficiency exceeding 9%," Sci. Rep. **2**, 591 (2012).
[3]M. M. Lee, J. Teuscher, T. Miyasaka, T. N. Murakami, and H. J. Snaith, "Efficient hybrid solar cells based on meso-superstructured organometal halide perovskites," Science **338**, 643–647 (2012).
[4]NREL, see https://www.nrel.gov/pv/cell-efficiency.html for "Best Research-Cell Efficiency Chart" (accessed August 4, 2022).
[5]G. E. Eperon, V. M. Burlakov, P. Docampo, A. Goriely, and H. J. Snaith, "Morphological control for high performance, solution-processed planar heterojunction perovskite solar cells," Adv. Funct. Mater. **24**, 151–157 (2014).
[6]Z. Xiao, C. Bi, Y. Shao, Q. Dong, Q. Wang, Y. Yuan, C. Wang, Y. Gao, and J. Huang, "Efficient, high yield perovskite photovoltaic devices grown by interdiffusion of solution-processed precursor stacking layers," Energy Environ. Sci. **7**, 2619–2623 (2014).
[7]M. Liu, M. B. Johnston, and H. J. Snaith, "Efficient planar heterojunction perovskite solar cells by vapour deposition," Nature **501**, 395–398 (2013).
[8]K. Wojciechowski, M. Saliba, T. Leijtens, A. Abate, and H. J. Snaith, "Sub-150 °C processed meso-superstructured perovskite solar cells with enhanced efficiency," Energy Environ. Sci. **7**, 1142–1147 (2014).
[9]See https://www.oxfordpv.com/news/oxford-pv-completes-build-out-its-brandenburg-factory for "Oxford PV" (accessed March 8, 2022) (2021).
[10]H. J. Snaith, "Present status and future prospects of perovskite photovoltaics," Nat. Mater. **17**, 372–376 (2018).
[11]A. Babayigit, A. Ethirajan, M. Muller, and B. Conings, "Toxicity of organometal halide perovskite solar cells," Nat. Mater. **15**, 247–251 (2016).
[12]H. J. Snaith, A. Abate, J. M. Ball, G. E. Eperon, T. Leijtens, N. K. Noel, S. D. Stranks, J. Tse-Wei Wang, K. Wojciechowski, and W. Zhang, "Anomalous hysteresis in perovskite solar cells," J. Phys. Chem. Lett. **5**, 1511–1515 (2014).
[13]S. N. Habisreutinger, N. K. Noel, and H. J. Snaith, "Hysteresis index: A figure without merit for quantifying hysteresis in perovskite solar cells," ACS Energy Lett. **3**, 2472–2476 (2018).
[14]J. M. Cave, N. E. Courtier, I. A. Blakborn, T. W. Jones, D. Ghosh, K. F. Anderson, L. Lin, A. A. Dijkhoff, G. J. Wilson, K. Feron, M. Saiful Islam, J. M. Foster, G. Richardson, and A. B. Walker, "Deducing transport properties of mobile vacancies from perovskite solar cell characteristics," J. Appl. Phys. **128**, 184501 (2020).
[15]S. Van Reenen, M. Kemerink, and H. J. Snaith, "Modeling anomalous hysteresis in perovskite solar cells," J. Phys. Chem. Lett. **6**, 3808–3814 (2015).
[16]G. Richardson, S. E. J. O'Kane, R. G. Niemann, T. A. Peltola, J. M. Foster, P. J. Cameron, and A. B. Walker, "Can slow-moving ions explain hysteresis in the current–voltage curves of perovskite solar cells?," Energy Environ. Sci. **9**, 1476–1485 (2016).
[17]N. E. Courtier, J. M. Cave, J. M. Foster, A. B. Walker, and G. Richardson, "How transport layer properties affect perovskite solar cell performance: Insights from a coupled charge transport/ion migration model," Energy Environ. Sci. **12**, 396–409 (2019).
[18]A. Riquelme, L. J. Bennett, N. E. Courtier, M. J. Wolf, L. Contreras-Bernal, A. B. Walker, G. Richardson, and J. A. Anta, "Identification of recombination losses and charge collection efficiency in a perovskite solar cell by comparing impedance response to a drift-diffusion model," Nanoscale **12**, 17385–17398 (2020).
[19]N. Tessler and Y. Vaynzof, "Insights from device modeling of perovskite solar cells," ACS Energy Lett. **5**, 1260–1270 (2020).
[20]J. Wei, Y. Zhao, H. Li, G. Li, J. Pan, D. Xu, Q. Zhao, and D. Yu, "Hysteresis analysis based on the ferroelectric effect in hybrid perovskite solar cells," J. Phys. Chem. Lett. **5**, 3937–3945 (2014).
[21]J. M. Frost, K. T. Butler, and A. Walsh, "Molecular ferroelectric contributions to anomalous hysteresis in hybrid perovskite solar cells," APL Mater. **2**, 081506 (2014).
[22]C. Li, S. Tscheuschner, F. Paulus, P. E. Hopkinson, J. Kießling, A. Köhler, Y. Vaynzof, and S. Huettner, "Iodine migration and its effect on hysteresis in perovskite solar cells," Adv. Mater. **28**, 2446–2454 (2016).
[23]C. Eames, J. M. Frost, P. R. F. Barnes, B. C. O'Regan, A. Walsh, and M. S. Islam, "Ionic transport in hybrid lead iodide perovskite solar cells," Nat. Commun. **6**, 7497 (2015).
[24]C. Jacoboni, *Theory of Electron Transport in Semiconductors: A Pathway From Elementary Physics to Nonequilibrium Green Functions* (Springer Science & Business Media, 2010), Vol. 165.
[25]T. Grasser, T. Ting-Wei, H. Kosina, and S. Selberherr, "A review of hydrodynamic and energy-transport models for semiconductor device simulation," Proc. IEEE **91**, 251–274 (2003).

[26]P. Calado, A. M. Telford, D. Bryant, X. Li, J. Nelson, B. C. O'Regan, and P. R. Barnes, "Evidence for ion migration in hybrid perovskite solar cells with minimal hysteresis," Nat. Commun. **7**, 1–10 (2016).
[27]N. E. Courtier, G. Richardson, and J. M. Foster, "A fast and robust numerical scheme for solving models of charge carrier transport and ion vacancy motion in perovskite solar cells," Appl. Math. Modell. **63**, 329–348 (2018).
[28]P. Calado, I. Gelmetti, B. Hilton, M. Azzouzi, J. Nelson, and P. R. F. Barnes, "Driftfusion: An open source code for simulating ordered semiconductor devices with mixed ionic-electronic conducting materials in one dimension," J. Comput. Electron. **21**, 960–991 (2022).
[29]N. E. Courtier, J. M. Cave, A. B. Walker, G. Richardson, and J. M. Foster, "IonMonger: A free and fast planar perovskite solar cell simulator with coupled ion vacancy and charge carrier dynamics," J. Comput. Electron. **18**, 1435–1449 (2019).
[30]N. E. Courtier, J. M. Foster, S. E. J. O'Kane, A. B. Walker, and G. Richardson, "Systematic derivation of a surface polarisation model for planar perovskite solar cells," Eur. J. Appl. Math. **30**, 427–457 (2019).
[31]S. Ravishankar, O. Almora, C. Echeverría-Arrondo, E. Ghahremanirad, C. Aranda, A. Guerrero, F. Fabregat-Santiago, A. Zaban, G. Garcia-Belmonte, and J. Bisquert, "Surface polarization model for the dynamic hysteresis of perovskite solar cells," J. Phys. Chem. Lett. **8**, 915–921 (2017).
[32]D. Moia, I. Gelmetti, P. Calado, W. Fisher, M. Stringer, O. Game, Y. Hu, P. Docampo, D. Lidzey, E. Palomares, J. Nelson, and P. R. F. Barnes, "Ionic-to-electronic current amplification in hybrid perovskite solar cells: Ionically gated transistor-interface circuit model explains hysteresis and impedance of mixed conducting devices," Energy Environ. Sci. **12**, 1296–1308 (2019).
[33]L. Bertoluzzi, C. C. Boyd, N. Rolston, J. Xu, R. Prasanna, B. C. O'Regan, and M. D. McGehee, "Mobile ion concentration measurement and open-access band diagram simulation platform for halide perovskite solar cells," Joule **4**, 109–127 (2020).
[34]A. J. Riquelme, K. Valadez-Villalobos, P. P. Boix, G. Oskam, I. Mora-Seró, and J. A. Anta, "Understanding equivalent circuits in perovskite solar cells. Insights from drift-diffusion simulation," Phys. Chem. Chem. Phys. **24**, 15657–15671 (2022).
[35]L. J. Bennett, A. Riquelme, N. E. Courtier, J. Anta, and G. Richardson, "Avoiding ionic interference in the computation of ideality factor for perovskite solar cells and an analytical theory for their impedance spectroscopy response," Phys. Rev. Appl. **19**, 014061 (2023).
[36]W. Tress, J. P. Correa Baena, M. Saliba, A. Abate, and M. Graetzel, "Inverted current-voltage hysteresis in mixed perovskite solar cells: Polarization, energy barriers, and defect recombination," Adv. Energy Mater. **6**, 1600396 (2016).
[37]Y. Rong, Y. Hu, S. Ravishankar, H. Liu, and X. Hou, "Tunable hysteresis effect for perovskite solar cells," Energy Environ. Sci. **10**, 2383–2391 (2017).
[38]E. Jokar, H.-S. Chuang, C.-H. Kuan, H.-P. Wu, C.-H. Hou, J.-J. Shyue, and E. Wei-Guang Diau, "Slow passivation and inverted hysteresis for hybrid tin perovskite solar cells attaining 13.5% via sequential deposition," J. Phys. Chem. Lett. **12**, 10106–10111 (2021).
[39]F. Wu, B. Bahrami, K. Chen, S. Mabrouk, R. Pathak, Y. Tong, X. Li, T. Zhang, R. Jian, and Q. Qiao, "Bias-dependent normal and inverted J–V hysteresis in perovskite solar cells," ACS Appl. Mater. Interfaces **10**, 25604–25613 (2018).
[40]E. Erdenebileg, L. E. Scholz, A. Hofacker, C. Koerner, and K. Leo, "Very small inverted hysteresis in vacuum-deposited mixed organic–inorganic hybrid perovskite solar cells," Energy Technol. **5**, 1606–1611 (2017).
[41]G. A. Nemnes, C. Besleaga, V. Stancu, D. E. Dogaru, L. N. Leonat, L. Pintilie, K. Torfason, M. Ilkov, A. Manolescu, and I. Pintilie, "Normal and inverted hysteresis in perovskite solar cells," J. Phys. Chem. C **121**, 11207–11214 (2017).
[42]F. Wu, R. Pathak, K. Chen, G. Wang, B. Bahrami, Wen-Hua Zhang, and Q. Qiao, "Inverted current–voltage hysteresis in perovskite solar cells," ACS Energy Lett. **3**, 2457–2460 (2018).
[43]N. E. Courtier, "Modelling ion migration and charge carrier transport in planar perovskite solar cells," Ph.D. thesis (School of Mathematical Sciences University of Southampton, 2019).
[44]D. A. Jacobs, Y. Wu, H. Shen, C. Barugkin, F. J. Beck, T. P. White, K. Weber, and K. R. Catchpole, "Hysteresis phenomena in perovskite solar cells: The many and varied effects of ionic accumulation," Phys. Chem. Chem. Phys. **19**, 3094–3103 (2017).
[45]H. Shen, D. A. Jacobs, Y. Wu, T. Duong, J. Peng, X. Wen, X. Fu, S. K. Karuturi, T. P. White, K. Weber, and K. R. Catchpole, "Inverted hysteresis in CH3NH3PbI3 solar cells: Role of stoichiometry and band alignment," J. Phys. Chem. Lett. **8**, 2672–2680 (2017).
[46]R. García-Rodríguez, A. J. Riquelme, M. Cowley, K. Valadez-Villalobos, G. Oskam, L. J. Bennett, M. J. Wolf, L. Contreras-Bernal, P. J. Cameron, A. B. Walker, and J. A. Anta, "Inverted hysteresis in n–i–p and p–i–n perovskite solar cells," Energy Technol. **10**, 2200507 (2022).
[47]C. Gonzales, A. Guerrero, and J. Bisquert, "Transition from capacitive to inductive hysteresis: A neuron-style model to correlate I–V curves to impedances of metal halide perovskites," J. Phys. Chem. C **126**, 13560–13578 (2022).
[48]J. Bisquert, A. Guerrero, and C. Gonzales, "Theory of hysteresis in halide perovskites by integration of the equivalent circuit," ACS Phys. Chem. Au **1**, 25–44 (2021).
[49]M. Minbashi and E. Yazdani, "Comprehensive study of anomalous hysteresis behavior in perovskite-based solar cells," Sci. Rep. **12**, 1–14 (2022).
[50]D. Abdel, P. Vágner, J. Fuhrmann, and P. Farrell, "Modelling charge transport in perovskite solar cells: Potential-based and limiting ion depletion," Electrochim. Acta **390**, 138696 (2021).
[51]A. Castro-Chong, A. J. Riquelme, T. Aernouts, L. J. Bennett, G. Richardson, G. Oskam, and J. A. Anta, "Illumination intensity dependence of the recombination mechanism in mixed perovskite solar cells," ChemPlusChem **86**, 1347–1356 (2021).
[52]M. T. Neukom, A. Schiller, S. Züfle, E. Knapp, J. Ávila, D. Pérez-del-Rey, C. Dreessen, K. P. S. Zanoni, M. Sessolo, H. J. Bolink, and B. Ruhstaller, "Consistent device simulation model describing perovskite solar cells in steady-state, transient, and frequency domain," ACS Appl. Mater. Interfaces **11**, 23320–23328 (2019).
[53]S. D. Stranks, V. M. Burlakov, T. Leijtens, J. M. Ball, A. Goriely *et al.*, "Recombination kinetics in organic-inorganic perovskites: Excitons, free charge, and subgap states," Phys. Rev. Appl. **2**, 034007 (2014).
[54]D. Bryant, S. Wheeler, B. C. O'Regan, T. Watson, P. R. F. Barnes, D. Worsley, and J. Durrant, "Observable hysteresis at low temperature in 'hysteresis free' organic–inorganic lead halide perovskite solar cells," J. Phys. Chem. Lett. **6**, 3190–3194 (2015).
[55]X. Wang, K. Rakstys, K. Jack, H. Jin, J. Lai, H. Li, C. S. K. Ranasinghe, J. Saghaei, G. Zhang, P. L. Burn, I. R. Gentle, and P. E. Shaw, "Engineering fluorinated-cation containing inverted perovskite solar cells with an efficiency of 21% and improved stability towards humidity," Nat. Commun. **12**, 52 (2021).
[56]E. Aydin, J. Liu, E. Ugur, R. Azmi, G. T. Harrison, Y. Hou, B. Chen, S. Zhumagali, M. De Bastiani, M. Wang, W. Raja, T. G. Allen, A. U. Rehman, A. S. Subbiah, M. Babics, A. Babayigit, F. H. Isikgor, K. Wang, E. Van Kerschaver, L. Tsetseris, E. H. Sargent, F. Laquai, and S. De Wolf, "Ligand-bridged charge extraction and enhanced quantum efficiency enable efficient n–i–p perovskite/silicon tandem solar cells," Energy Environ. Sci. **14**, 4377–4390 (2021).
[57]Y. Zhang and N.-G. Park, "Quasi-two-dimensional perovskite solar cells with efficiency exceeding 22%," ACS Energy Lett. **7**, 757–765 (2022).